Soft Matter

Cite this: *Soft Matter*, 2011, **7**, 9216

www.rsc.org/softmatter

PAPER

Kinetics of coalescence in liquid aluminium foams

F. Garcia-Moreno,*[ab] E. Solórzano[ac] and J. Banhart[ab]

Received 5th May 2011, Accepted 19th July 2011
DOI: 10.1039/c1sm05831b

The cell wall rupture kinetics for a collection of AlSi9 foam samples kept at a constant temperature over the melting point for a long time period (700 s) has been characterized by *in situ* X-ray radioscopy. The images obtained have been computed by using image analysis algorithms allowing the identification of the cell wall ruptures in the molten state. The time evolution, the spatial distribution and the number of cell wall rupture events are studied in this work. The cell wall rupture rate was determined for the first time in liquid aluminium foams. Part of the results obtained has been explained in terms of the spatial distribution of temperature obtained by different heating configurations and measured by thermographic techniques. The progressive coarsening and density redistribution of the cellular structure and the drainage due to gravity have been also considered. The local temperature seems to be critical for the rupture phenomena and the temperature distribution clearly affects the foam density distribution.

1 Introduction

Liquid metal foams are fragile systems and prone to gravity-driven drainage and coalescence of bubbles. If this happens excessively before solidification, the morphology and the properties of the resulting solid foam will be compromised by the resulting density gradients and the on average larger and less uniformly distributed cells.[1] Therefore it is worth studying drainage and coalescence and to identify the factors that control these deleterious effects.

The behaviour of liquid metal foam has been investigated in a number of studies. The foam melting and expansion,[2,3] foam solidification,[4] the gas release properties of the blowing agent[5–7] and their impact on foaming[8,9] have been characterised quantitatively. Drainage in liquid metal foam has been studied both on Earth[10] and under microgravity conditions.[11,12] Coalescence of cells has been observed by using *in situ* imaging techniques such as X-ray radioscopy.[13–16] These *in situ* methods are essential to reveal the temporal evolution of metal foams from pore nucleation and bubble growth to foam decay. In contrast, the nature of metal foam stabilisation, namely networks of oxides provided by the metallic powders, has been studied *ex situ* on solidified foams by using microscopy techniques.[17–20]

As possible reasons for coalescence the loss of a material due to drainage—leading to film thinning—or mechanical stresses due to bubble expansion or rearrangement has been proposed.[17,21] In addition, rupture phenomena can be triggered by solidification.[22–24] Microgravity experiments have shown that even in the absence of drainage and any visible macroscopic foam expansion coalescence can be observed, which could be partially ascribed to non-uniform gas generation by the individual blowing agent particles caused by their variation in size and distribution within the precursor.[12] In addition, temperature gradients are likely to give rise to pressure differences between adjacent bubbles that then lead to film shear and rupture. To verify and quantify the influence of temperature gradients on coalescence is the main topic of the present work. The authors have previously demonstrated that infrared thermography is suitable for measuring the temperature distribution in evolving metallic foams *in situ* if certain conditions are satisfied.[25] The combination with *in situ* X-ray radioscopy applied in this work allows us to link temperature distributions with cell wall rupture distributions.

2 Experimental

2.1 Materials and furnaces

A foamable precursor material of the composition AlSi9 containing 0.6 wt% of TiH_2 was used for the experiments. The precursor was manufactured by uni-axial hot compaction of a powder blend of the elemental metallic powders and the blowing agent. The consolidation was achieved applying 300 MPa at 400 °C for 5 min. Pieces of the material were inserted into a square stainless steel section—cross-section 30 × 30 mm^2, length 28 mm, wall thickness 3 mm—which served as a mould. The two open sides were covered with 25 μm thick stainless steel foil, which does not substantially affect X-ray imaging due to its

[a]*Institute of Applied Materials, Helmholtz Centre Berlin for Materials and Energy, Hahn-Meitner-Platz 1, 14109 Berlin, Germany. E-mail: garcia-moreno@helmholtz-berlin.de*
[b]*Institute of Materials Science and Technology, Technische Universität Berlin, Hardenbergstrasse 36, 10623 Berlin, Germany*
[c]*CellMat Group, Condensed Matter Physics Department, Science Faculty, Universidad de Valladolid, Prado de la Magdalena S/N, 47011 Valladolid, Spain*

weak absorption, but provides two important functions: it constrains foam expansion in the direction of the X-rays and therefore avoids an increase of the sample thickness and—in the thermographic measurements—serves as a screen of constant emissivity which is essential to obtain meaningful temperature readings.[25]

Two different heating conditions were applied to promote dissimilar temperature distributions within the liquid metal foam (see Fig. 1). First, homogeneous heating conditions were realised by using three near/mid infrared heating lamps—*top*, *left* and *right*—to heat the mould and thus, indirectly, the sample (Fig. 1a). This condition was expected to produce nearly homogeneous temperature distributions in the foam although the bottom of the mould was not directly heated. However, a large part of the heat was transferred through the left and right sides of the mould into the foam due to the direct metal/metal contact. The infrared heating lamps did not influence the temperature reading of the infrared camera since they emit in a different spectral range. Inhomogeneous heating (Fig. 1b) was achieved by using a resistive ceramic heater as a source that heated the mould from the bottom only. The intention of this was to deliberately produce a temperature gradient from the bottom to the top. The two heating conditions were controlled in such a way that a similar average temperature was obtained in both cases.

X-Ray and infrared thermography experiments could not be carried out simultaneously, but were performed in replicated experiments under identical conditions.

2.2 X-Ray radioscopy

A laboratory X-ray set-up allowed us to record the foaming process *in situ*. A tungsten anode micro-focus X-ray source and a flat panel detector were used, both from Hamamatsu, Japan.[15] The X-ray emission originated from a spot of 5 μm diameter. The panel detector had a pixel size of 50 μm. Applying a 4-fold magnification, each pixel contained image information from a sample area of 12.5 × 12.5 μm^2 for all the experiments. 2D-projected images of 2240 × 2368 $pixel^2$ were recorded every 2 s. These images were the source for the quantitative analysis performed with the dedicated software package 'Axim'. It allows beside the foam expansion calculation described elsewhere[15] and drainage analysis—*i.e.* density distribution described later—as well as the analysis of the number and (x,z)-coordinates of cell wall ruptures.

For the analysis of cell wall rupture, consecutive X-ray images are subtracted and compared with each other with the aim to detect localized image changes above a given threshold. Possible artefacts caused by the effect of local drifts due to topological rearrangements of cell walls are eliminated by comparing them with their direct neighbourhood. Shifts of interconnected pixels are detected, verified as true changes of the foam structure, labelled and interpreted as a single cluster. Finally, adjacent clusters are merged together and the (x,z)-coordinates of the pixels involved are averaged to obtain a coordinate corresponding to a single rupture event, which depends on adjustable distance parameters. The example in Fig. 2 illustrates the detection of three ruptures in two consecutive images.

A quantitative analysis of cell wall rupture could be performed only after foam expansion had completed and the liquid metal foam reached its maximal expansion since before this instant the macroscopic movement of features within the foam produced too many artefacts. Therefore, rupture analysis could only be performed for the period between 500 and 1200 s after heating had started, *i.e.* for a period of 700 s in the expanded liquid condition. After adjustment of the software parameters, the number of rupture events detected automatically represented true ruptures in 98% of all cases as verified by visual inspection. Each analysis was based on two independent experiments.

The software 'Axim' also provides the 2D density projection of the evolving foam ($\rho_{foam}(x,z)$) from the intensity $I(x,z)$ obtained from the radiographs and by applying Beer–Lambert's attenuation law:

$$I(x,z) = I_0 e^{-\mu \rho_{foam}(x,z) d}. \quad (1)$$

From this, the relative density distribution of the foam $\rho_{rel}(x,z) = \rho_{foam}(x,z)/\rho_{bulk}(x,z)$ can be calculated, assuming that the foam depth d in the beam direction is kept constant. μ is the mass-specific absorption coefficient of the base alloy and I_0 the initial beam intensity. One obtains

$$\rho_{rel}(x,z,t) = \frac{\ln\left(I(x,z,t)/I_0\right)}{\ln\left(I_{bulk}/I_0\right)}, \quad (2)$$

where I_{bulk} is the intensity after attenuation by the unfoamed metal precursor of equal thickness d. As the main interest lies on the vertical density profile, the pixel values in the horizontal direction are added up to:

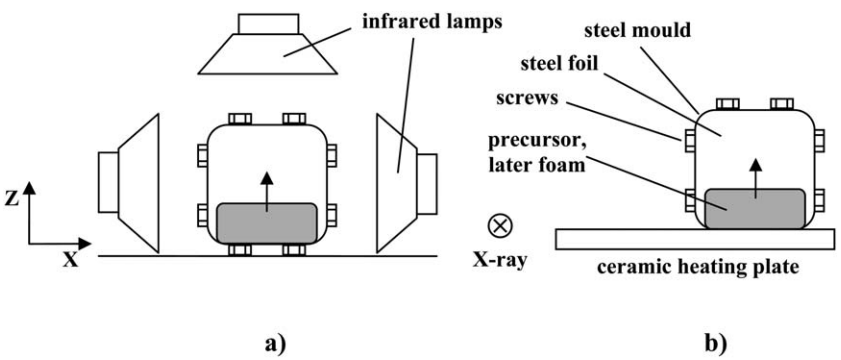

Fig. 1 Scheme of the heating setup applied: (a) homogeneous and (b) inhomogeneous heating.

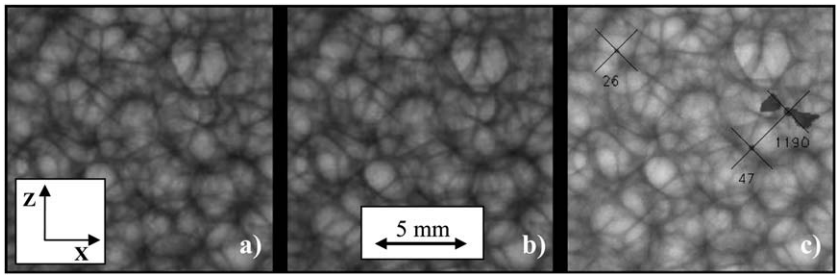

Fig. 2 (a and b) Selected areas of two consecutive X-ray radiographs ($\Delta t = 2$ s). (c) Illustration of the corresponding cell wall ruptures detected using 'Axim', showing the number of pixels corresponding to clusters of a single event and the centre of the event superimposed on (b).

$$\rho_{\mathrm{rel}}(z,t) = \frac{\ln\left(\frac{1}{n}\sum_{x=0}^{n} I(x,z,t)/I_0\right)}{\ln\left(I_{\mathrm{bulk}}/I_0\right)} \quad (3)$$

Using this equation, the density distribution in the foam throughout the entire process can be obtained and effects such as gravity-induced drainage discussed. An example of this technique with changing density distributions and drainage has been given previously.[11]

2.3 Far-infrared thermography

A far-infrared camera model 'Thermovision A40M' by Flir-Systems was used to acquire the surface temperature of the samples during foaming. The spatial temperature resolution is defined by a 320 × 240 microbolometer detector matrix with a pixel size of 50 × 50 μm^2. Thermographic images were acquired at 12.5 fps whereas the other experimental conditions were kept the same as reported previously.[25] Thermocouples were used to measure the real temperature in order to calibrate the emissivity of the samples monitored. This procedure enables a reliable temperature monitoring through the local temperature adjustment of a surface with homogeneous emissivity.[25]

The measured images were analyzed using the software 'ImageJ'[26] taking account of the pixel value calibration with temperature, the real pixel size and the time gap between the frames. The temperature profiles of the foam kept at the foaming temperature were determined from such images. The resulting thermographies, see Fig. 3, show a nearly constant temperature gradient along the z-direction when lamps were used for heating (Fig. 3a), whereas inhomogeneous heating gave rise to visible gradients (Fig. 3b).

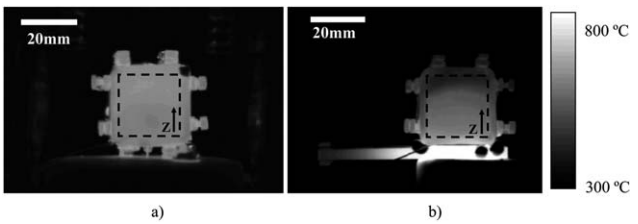

Fig. 3 Thermal images of samples kept at the foaming temperature after (a) homogeneous and (b) inhomogeneous heating.

3 Results and analysis

First, the temperature distributions determined using the IR camera are reported. They provide a basis for the interpretation of the X-ray radioscopic experiments. Based on these experiments on liquid foams, both the drainage process (given as a function of time and vertical position) and the process of coalescence (spatial distribution) are quantified for both heating conditions.

3.1 Temperature distributions

The thermographs obtained exhibit a notable temperature variation only in the vertical direction. The temperature profiles are constant in the horizontal direction as shown in Fig. 3. The temperature distribution after completion of expansion no longer evolves with time when the foam is kept at an average constant temperature. Such stationary temperature distributions along the z-direction in the marked rectangle, see Fig. 3, are given in Fig. 4 for both heating configurations. The maximum difference in temperature from the bottom to the top is lower than 25 K when lamps were used for homogeneous heating. In contrast, inhomogeneous heating yields a much higher and almost linear temperature gradient from the bottom to the top. A pronounced temperature drop is found in the top part, which is a measurement artefact related to the missing contact between

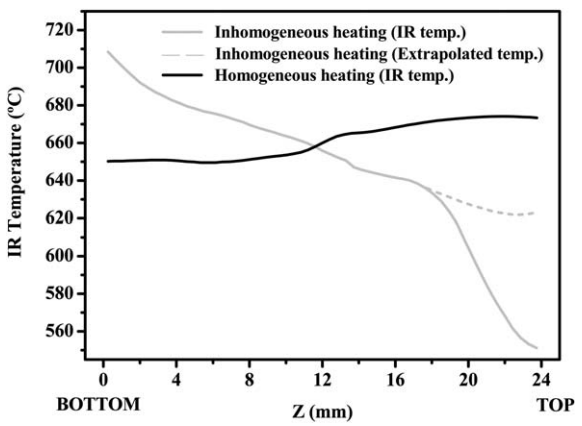

Fig. 4 Vertical temperature profiles of a foam heated homogeneously (left) or inhomogeneously (right). The broken line in the profile indicates an extrapolated temperature in a region where the foam no longer touched the steel foil.

the foam and the steel foil. The temperature in this area is much lower than expected and the IR camera even gave unrealistic values below the melting point of the metal. An extrapolated temperature profile that is considered more realistic is displayed in Fig. 4. Accordingly, the maximum temperature difference from bottom to top is about 90 K. Despite the difference between the two heating conditions, the average of the temperature profile is almost the same, close to 660 °C.

3.2 X-Ray radioscopy

In Fig. 5, some radiographs of the expanding foam obtained *in situ* at different times are reproduced for the two heating conditions. For $t = 400$ s, the foams were just about to fill the mould. For the homogeneous heating condition, a higher density at the bottom is observed at this time, other than for inhomogeneous heating, where the foam is denser at the top. For $t = 800$ and 1200 s, a vertical density gradient emerges, which points at gravity-induced drainage. This drainage effect is more pronounced for inhomogeneous heating. Pore coarsening, *i.e.* gradual growth of bigger pores at the cost of smaller ones due to gas diffusion, was not observed for any of the conditions.

3.3 Density profile

The density profile is constant in the horizontal direction as it can be observed in Fig. 5. Fig. 6 shows the time evolution of the density distribution along the z-direction for the two heating conditions after the foam had reached full expansion. At around $t = 500$ s, some slight drainage has already increased the density at the bottom (~5 to 7 mm) of the foam. The density of the remaining foam was close to an average level of ~10 to 20% of the full metal density. Up to this point there were no significant differences between both heating conditions, but for longer times, a drainage-related non-uniformity emerged. This happened more immediately for the inhomogeneous heating condition, and led to an accumulation of the liquid metal at the bottom of the foam indicated by arrows in Fig. 6. For the remaining time up to 1200 s, the density at the bottom increased continuously up to 40% and 60% for the homogeneous and inhomogeneous conditions, respectively.

3.4 Rupture analysis

Rupture maps visualising the location of all events detected by image analysis are shown in Fig. 7. Each dot corresponds to a detected rupture event that occurred at any time such as the one marked with a cross in Fig. 2. In addition, vertical and horizontal rupture density profiles are attached to the maps to facilitate interpretation. The existence of a non-uniform rupture distribution is clearly observed in both these graphs. The ruptures for the homogeneous heating condition are uniformly distributed, except for some rupture clusters in the top part. In the horizontal direction, no preference can be detected. For the inhomogeneous heating conditions, rupture was much more frequent at the bottom of the foam except for the bottommost 3 mm, where only very few events were observed. There is a slight horizontal gradient.

4 Discussion

4.1 Spatial distribution of rupture events

The rupture distribution displayed as a 2D rupture map in Fig. 7 demonstrates that rupture events are not uniformly distributed in the vertical direction, suggesting an influence of the temperature profile—oriented in the z-direction too, see Fig. 4—and/or of gravitational drainage, see Fig. 6. Both the rupture density gradient as well as the temperature gradient are higher for inhomogeneous heating, where the bottom part of the foam is hotter and more ruptures are observed. For homogeneous heating, the top part is slightly hotter and there are more ruptures, see Fig. 7a. These qualitative observations point at a direct correlation between the temperature and rupture density

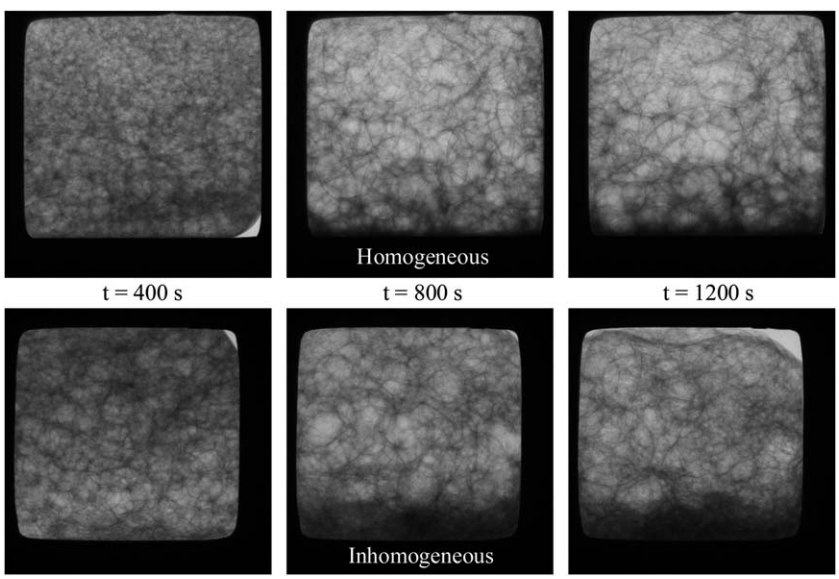

Fig. 5 X-Ray radiographs of expanding foams, $t = 400$, 800 and 1200 s after the beginning of heating for homogeneous (top) and inhomogeneous (bottom) heating conditions.

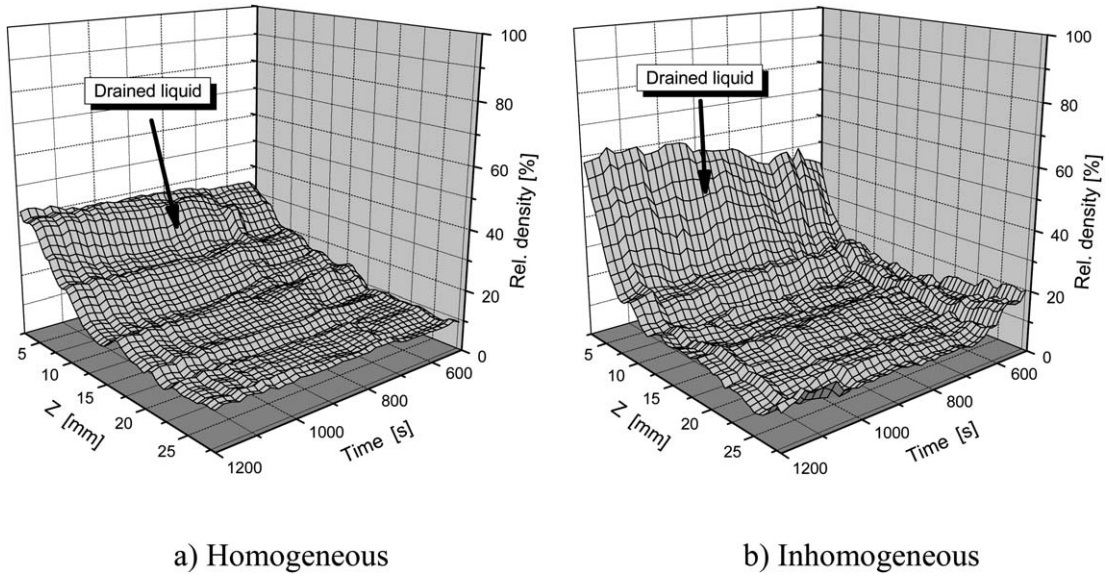

Fig. 6 Relative foam density as a function of foam height z and time for the two heating conditions applied, starting at $t = 500$ s after the beginning of heating. At this time, the mould just has been filled by the foam. Arrows indicate higher densities in the foam of the bottom part caused by drained liquid.

(higher temperature leads to a higher number of ruptures). A quantitative approach and possible reasons will be discussed later.

In the literature on aqueous foams it is assumed that enhanced rupture activity—*i.e.* coarsening—is produced by gravity-induced drainage with a following cell wall thinning and density decrease at the top of a column of foam.[27–29] For metal foams, investigations have shown that the total rupture rate of a liquid metal foam under microgravity conditions is similar to that under gravity, although locally depending on density.[12]

At the very bottom part of the samples very few ruptures are observed in both experiments. This is because gravity-induced drainage gives rise to a dense region in both conditions within the period this rupture analysis is carried out, see Fig. 6. As the foam becomes denser, fewer pores and thicker cell walls are found and rupture less likely. Especially for inhomogeneous heating, this region is very pronounced. We conclude that this is caused by the elevated temperatures there, which lead to stronger drained liquid and to many ruptures already during foam growth, *i.e.* before rupture analysis started. This fact was observed in the X-ray images.

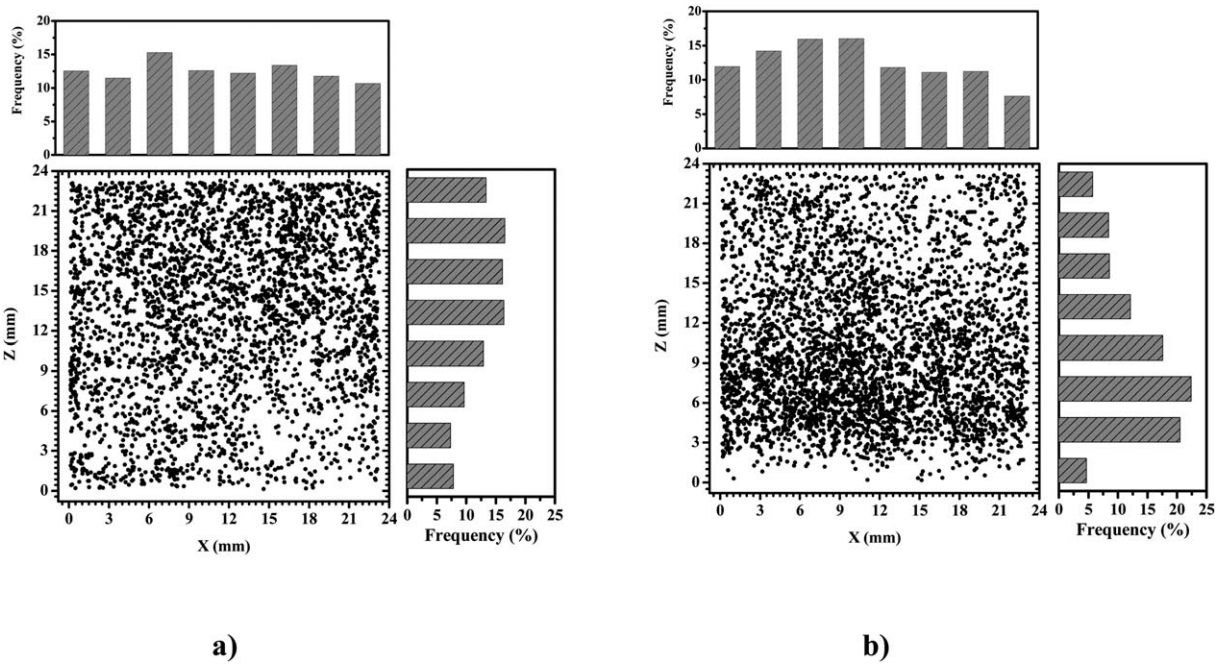

Fig. 7 Rupture maps and vertical and horizontal rupture distribution histograms for (a) homogeneous and (b) inhomogeneous heating conditions. Each graph contains data from 2 experiments.

The temperature gradient from bottom to top for the inhomogeneous heating condition (Fig. 4) is responsible for a retardation of foaming and a higher density at the top as seen in Fig. 6b and from the image sequences in Fig. 5. The melt viscosity can be thought to be reduced at the bottom because of the increased temperature, which may also increase the rupture rate. The higher temperature also contributes to liquid accumulation and leads to an increase of 20% in maximum density for the inhomogeneous case compared to normal drainage for the homogeneous condition.

4.2 Time evolution of the rupture process

A rupture rate analysis corresponds to an analysis of the pore coalescence, and thus of the evolution of the mean pore size. This rate is nearly constant for the volume studied throughout the monitoring time (700 s), as shown in Fig. 8. Therefore, the mean pore size is increasing in time while the absolute pore number decreases. Opposite as for polydispersed aqueous foams, coarsening due to gas diffusion between the bubbles was not found, which is typical for metallic foams.[13] Therefore, the mean pore size in a fully expanded metal foam should only be affected by the cell wall rupture kinetics.

4.3 Correlation of rupture rate and temperature

It has been shown that both the temperature and the rupture frequency depend on the vertical position. Values for the local temperature, for the rupture frequency and for the time interval are available. The rupture frequency f shown as a 2D map in Fig. 7 is a projection of ruptures in the entire foam volume and can be used to derive a rupture rate n. The vertical direction was divided into segments and the average temperature and the total number of ruptures in each segment were determined. Each segment corresponds to a defined volume since the sample is contained in a mould of a fixed depth. The total time of the experiment is also known, enabling to calculate the rupture rate density $\bar{n}$ or, in other words, the average number of ruptures per volume V and time t. It can be given as a function of average temperature $\bar{T}$:

$$\bar{n}(\bar{T}) = \frac{f}{tV}(\bar{T}). \quad (4)$$

The calculated data are displayed in Fig. 9.

A linear correlation between the normalized volume rupture rate and the averaged temperature can be found for most of the data. Only the results for inhomogeneous heating show deviations that can be explained in a following way: in the top part, the missing contact between the sample and the steel foil gave rise to a temperature reading that was lower than the actual temperature of the foam behind the foil (the shaded region labelled as *inhomogeneous top*). On the other hand, some of the ruptures at the bottom of the mould could not be detected since they either happened in a too early stage before starting monitoring at $t =$ 500 s or no foam was present anymore at this position due to strong early drainage. As a consequence, the point in the shaded region labelled as *inhomogeneous bottom* presents a reduced number of observed rupture events.

After disregarding these points for inhomogeneous heating, a linear fit represents the data points collected for the two heating conditions. This linear fit intersects the temperature axis (no rupture) at $T_0 = 615 \pm 5$ °C, which is very close to the liquidus temperature of the alloy (~623 °C). Therefore, eqn (4) can be written as:

$$\bar{n}(\bar{T}) = a(\bar{T} - T_0) \quad (5)$$

with a coefficient $a = 14.7 \pm 1.5 \times 10^{-3}$ s^{-1} K^{-1} cm^{-3}.

This fit corresponds to the average rupture rate in the analyzed time interval (700 s), short enough for being represented by a constant rupture rate and having a much larger number of cells compared to ruptures. In later stages the number of cells will be progressively reduced and the rupture rate will slowly tend to 0.

For the identification of possible mechanisms influencing coalescence kinetics and for explaining the relationship found in eqn (5), three possible mechanisms can be considered: change of melt viscosity, surface tension and gas release rate of the blowing agent.

The viscosity η of Al-alloys follows an Arrhenius–Andrade type temperature dependence, namely $\eta \propto e^{(1/T)}$, *i.e.* viscosity will

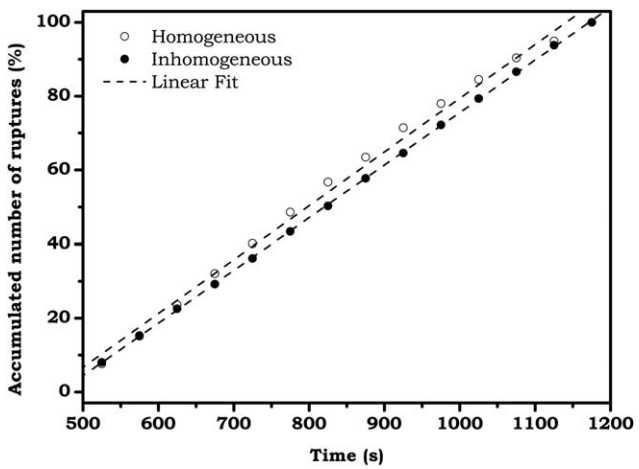

Fig. 8 Records of cumulative ruptures *versus* time, provided in relative frequency for a better comparison.

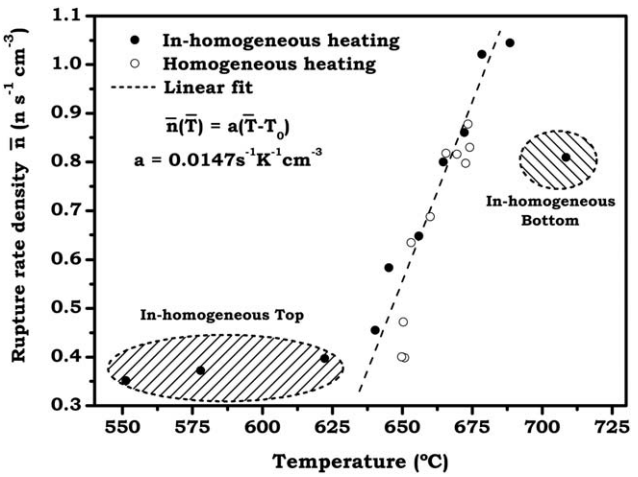

Fig. 9 Rupture rate density *vs.* average temperature for the two heating conditions applied, shaded regions are not fitted.

decrease with increasing temperature.[30] A decrease of melt viscosity has been related to a decrease of liquid metal foam stability, although without any quantitative relation to the rupture rate.[31,32] On the other hand, an enhancement of the melt viscosity was supposed to have a positive effect on foam stability.[31,33–35] This suspected effect was used by various foam production routes such as Cymat[33] by admixing ceramic particles to a melt, or Alporas[34] by adding Ca metal and producing CaO for melt thickening.[31,35] Nevertheless it is still not completely understood whether the admixed solid particles act due to their adherence to the melt/gas interface, or by increasing the apparent viscosity.[36,37] Further investigations on PM foams, where solid oxides from the metal powders are responsible for stabilization,[17] have shown that the cell wall rupture time is in the order of milliseconds or less, thus not dominated by viscosity.[16]

The surface tension σ of a similar alloy (AlSi8) was found to decrease with temperature linearly, so that $\sigma \propto 1/T$.[38] This indicates an increase of cell wall stability, opposite to our experimental findings. On the other hand we have to consider that metal films are stabilised by oxide networks also located in the cell wall surface.[17] The real value of the surface tension compared to the one of the pure melts might be different.

The gas pressure inside adjacent pores could be slightly different in the presence of temperature gradients just by considering the ideal law: $p \propto T$. This effect should be small, but could be largely enhanced by additional pressure gradients generated by locally differing gas production by some still active TiH_2 particles. These particles are very sensitive to temperature and strong gas release can be caused by slightly increasing the temperature.[9] Even in the case of homogeneous temperature distribution, ruptures could be triggered by this mechanism since TiH_2 particles are not uniformly distributed within the sample and act more likely point gas source. Moreover, different grain sizes could lead to varying gas release rates.

Nevertheless evidences are still not enough to verify that the temperature dependence of the rupture rate is dominated by only one of the proposed mechanisms or alternatively by a combination of them. Two of the proposed mechanisms—gas release rate and viscosity change—lead to the destabilisation of films with increasing temperature, whereas only surface tension would stabilize. The exact interplay between these three factors is not known, just the resulting effect: the increase of temperature destabilises films in metal foams.

4.4 Effect of ruptures on gravity-induced drainage

The rupture distribution along the vertical axis must have an effect on drainage as it has been demonstrated to be different under different heating conditions (local temperature correlated) (Fig. 6). Therefore, to precisely understand this phenomenon, we must consider two known facts: (i) drainage is gravity influenced, so the liquid amount at the bottom part of the foam has a natural tendency to increase with time and (ii) temperature contributes to accelerate liquid metal redistribution. Nevertheless the question is whether the temperature contribution on drainage is preferentially based on liquid flow (reduced viscosity within the cell walls facilitating the melt movement) or alternatively local ruptures are translated into local mass accumulation.

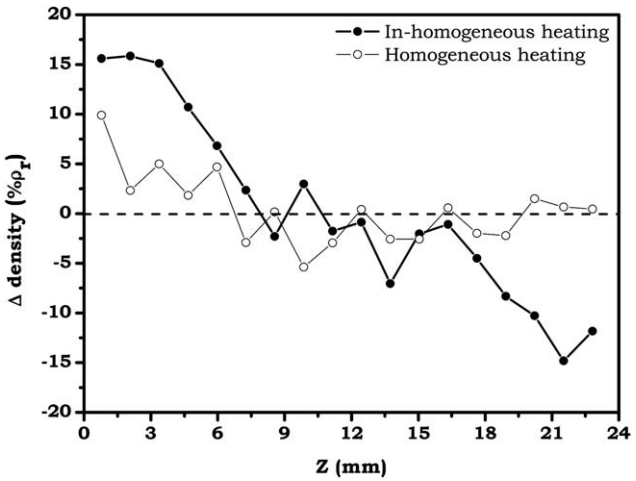

Fig. 10 Differences in the vertical density profiles ($\rho(z,t_2) - \rho(z,t_1)$) of the foam columns for inhomogeneous and homogeneous heating in the period between $t = 500$ s and $t = 1200$ s.

Fig. 10 shows the difference between the two density profiles after 1200 s (last) and 500 s (first), for both heating conditions. These curves represent the cumulated effect of drainage over this period. We can observe that significant amounts of liquid have flowed from the top to the bottom for the inhomogeneous heating condition. For uniform heating, a less pronounced liquid flow to the bottom also exists, although the temperature was higher at the top (Fig. 4). We also know where the ruptures were preferentially located (Fig. 7). Liquid displacement in the case of homogeneous conditions is poor and the top part does not reduce its relative density (even it is slightly increased) meanwhile

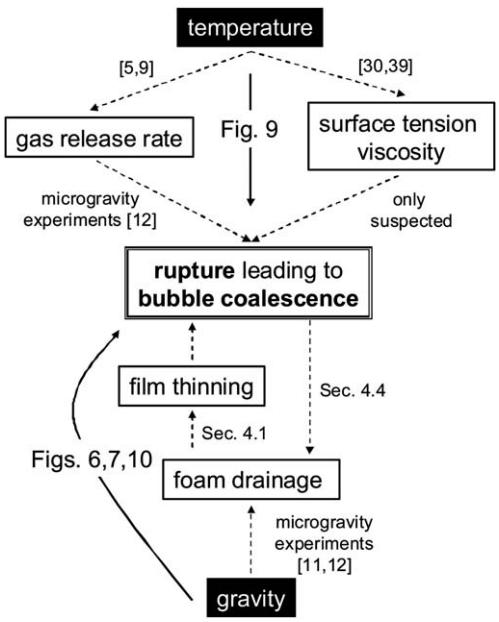

Fig. 11 Relationship between the two external stimuli gravity and temperature on the measured cell wall rupture behaviour of the metal foams. Full arrows identify our measurements. The inter-relationship between various materials properties or processes which is discussed in Section 4 is outlined by broken arrows and corresponding references.

the bottom is liquid-enriched by a contribution of the middle part of the foam, but not as much as for the inhomogeneous temperature case. These results point to an additional mechanism of liquid capture preferentially induced by ruptures which are correlated to temperature. This explains mass accumulation in the bottom of the inhomogeneous heated foam and leads to the conclusion that drainage not only influences coalescence, but it is influenced itself by cell wall ruptures in the relative short time-period studied. The complex relationship between the two main effects influencing the kinetics of coalescence in liquid metal foams, namely temperature and gravity, and the cell wall rupture is summarized in Fig. 11.

5 Conclusions

- Combination of X-ray radiography and infrared thermography has provided new insights into the temperature dependence of coalescence in metal foams.

- By applying homogeneous and inhomogeneous heating conditions, the influence of temperature gradients and drainage on coalescence could be studied.

- Over an analyzed time period of 700 s, the rupture rate density did not significantly change. Moreover, the rupture rate density was found to vary linearly with temperature.

- In the studied conditions the most presumable factors responsible for coalescence dependence with temperature are viscosity, surface tension and gas pressure gradients from the blowing agent.

- A part of the observed drained liquid in this relatively short time-period is caused by local coalescence, inducing local liquid accumulation.

6 Outlook

By means of X-ray radioscopy and additional normalisation of the absolute bubble number *e.g.* by *ex situ* tomography of solidified samples one could follow *in situ* the mean pore size evolution by following the cell wall ruptures.

Simultaneous *in situ* X-ray radioscopy and IR-thermography, using *e.g.* an IR-mirror and X-ray shielding for the IR camera, are feasible and could facilitate experiments.

Acknowledgements

The authors are grateful to the Spanish Ministry of Science and Education that supported the stay of E. Solórzano in Berlin with a FPU grant Ref-AP-2004-2908 and a postdoctoral grant REF-2008-0946. Funding by the European Space Agency ESA (Projects μg-FOAM AO-99-075) is also gratefully acknowledged.

References

1 K. Y. G. McCullough, N. A. Fleck and M. F. Ashby, *Acta Mater.*, 1999, **47**, 2323–2330.
2 I. Duarte and J. Banhart, *Acta Mater.*, 2000, **48**, 2349–2362.
3 D. Lehmhus and M. Busse, *Adv. Eng. Mater.*, 2004, **6**, 391–396.
4 M. Mukherjee, F. Garcia-Moreno and J. Banhart, *Acta Mater.*, 2010, **58**, 6358–6370.
5 B. Matijasevic-Lux, J. Banhart, S. Fiechter, O. Görke and N. Wanderka, *Acta Mater.*, 2006, **54**, 1887–1900.
6 D. Lehmhus and G. Rausch, *Adv. Eng. Mater.*, 2004, **6**, 313–330.
7 F. von Zeppelin, M. Hirscher, H. Stanzick and J. Banhart, *Compos. Sci. Technol.*, 2003, **63**, 2293–2300.
8 B. Matijasevic and J. Banhart, *Scr. Mater.*, 2006, **54**, 503–508.
9 C. Jiménez, F. Garcia-Moreno, B. Pfretzschner, M. Klaus, M. Wollgarten, I. Zizak, G. Schumacher, M. Tovar and J. Banhart, Acta Mater., in press, 2011, DOI: 10.1016/j.actamat.2011.06.042.
10 O. Brunke, A. Hamann, S. J. Cox and S. Odenbach, *J. Phys.: Condens. Matter*, 2005, **17**, 6353–6362.
11 F. García-Moreno, C. Jiménez, M. Mukherjee, P. Holm, J. Weise and J. Banhart, *Colloids Surf., A*, 2009, **344**, 101–106.
12 F. Garcia-Moreno, M. Mukherjee, C. Jimenez and J. Banhart, *Trans. Indian Inst. Met.*, 2009, **62**, 451–454.
13 J. Banhart, H. Stanzick, L. Helfen and T. Baumbach, *Appl. Phys. Lett.*, 2001, **78**, 1152–1154.
14 H. Stanzick, M. Wichmann, J. Weise, L. Helfen, T. Baumbach and J. Banhart, *Adv. Eng. Mater.*, 2002, **4**, 814–823.
15 F. García-Moreno, M. Fromme and J. Banhart, *Adv. Eng. Mater.*, 2004, **6**, 416–420.
16 F. García-Moreno, A. Rack, L. Helfen, T. Baumbach, S. Zabler, N. Babcsán, J. Banhart, T. Martin, C. Ponchut and M. Di Michiel, *Appl. Phys. Lett.*, 2008, **92**, 134104–134106.
17 C. Körner, M. Arnold and R. F. Singer, *Mater. Sci. Eng., A*, 2005, **396**, 28–40.
18 N. Babcsán, D. Leitlmeier and H. P. Degischer, *Materialwiss. Werkstofftech.*, 2003, **34**, 22–29.
19 J. Banhart, *Adv. Eng. Mater.*, 2006, **8**, 781–794.
20 A. Dudka, F. García-Moreno, N. Wanderka and J. Banhart, *Acta Mater.*, 2008, **56**, 3990–4001.
21 C. Körner, F. Berger, M. Arnold, C. Stadelmann and R. F. Singer, *Mater. Sci. Technol.*, 2000, **16**, 781–784.
22 M. Mukherjee, U. Ramamurty, F. Garcia-Moreno and J. Banhart, *Acta Mater.*, 2010, **58**, 5031–5042.
23 E. Solórzano, M. A. Rodríguez-Pérez and J. A. de Saja, in *Aluminum Alloys: their Physical and Mechanical Properties*,ed. J. Hirsch, B. Skrotzki and G. Gottstein, Wiley-VCH, 2008, vol. 2, pp. 2200–2206.
24 M. Mukherjee, F. Garcia-Moreno and J. Banhart, *Scr. Mater.*, 2010, **63**, 235–238.
25 E. Solórzano, F. Garcia-Moreno, N. Babcsán and J. Banhart, *Journal of Nondestructive Evaluation*, 2009, **28**, 141–148.
26 M. D. Abramoff, P. J. Magelhaes and S. J. Ram, *J. Biophoton. Int.*, 2004, **11**, 36–42.
27 C. Monnereau, M. Vignes-Adler and B. Kronberg, *J. Chem. Phys.*, 1999, **96**, 958–967.
28 A. Saint-Jalmes, *Soft Matter*, 2006, **2**, 836–849.
29 D. Weaire and S. Hutzler, *The Physics of Foams*, Clarendon Press, Oxford/New York, 1999.
30 A. T. Dinsdale and P. N. Quested, *J. Mater. Sci.*, 2004, **39**, 7221–7228.
31 Z.-L. Song, L.-Q. Ma, Z.-J. Wu and D.-P. Ge, *J. Mater. Sci.*, 2000, **35**, 15–20.
32 V. Gergely and T. W. Clyne, *Acta Mater.*, 2004, **52**, 3047–3058.
33 A.-M. Harte and S. Nichol, *Cellular Metals and Metal Foaming Technology*, ed. J. Banhart, M. F. Ashby and N. A. Fleck, MIT-Verlag, Bremen, 2001, pp. 49–55.
34 T. Miyoshi, *Metal Foams and Porous Metal Structures*, ed. J. Banhart, M. F. Ashby and N. A. Fleck, MIT-Verlag, Bremen, 1999, pp. 125–132.
35 S.-W. Ip, Y. Wang and J. M. Toguri, *Can. Metall. Q.*, 1999, **38**, 81–92.
36 A. Haibel, A. Rack and J. Banhart, *Appl. Phys. Lett.*, 2006, **89**, 154102–154104.
37 G. Kaptay, *Cellular Metals and Metal Foaming Technology*, ed. J. Banhart, N. A. Fleck and A. Mortensen, MIT-Verlag, Bremen, 2003, pp. 107–112.
38 J. Goicoechea, C. Garcia-Cordovilla, E. Louis and A. Pamies, *J. Mater. Sci.*, 1992, **27**, 5247–5252.